Nanoscale

PAPER

View Article Online
View Journal | View Issue



Cite this: *Nanoscale*, 2025, **17**, 10670

# Surface engineering of NIR-II luminescent gold nanoclusters for brain glioma-targeted imaging†

Shufen Tong,[a] Jie Liu,[a] Yonghui Chen,[a] Xinyun Xiao,[b] Shihua Li,*[b] Xiaorong Song *[a,c] and Huanghao Yang [a,c]

Received 7th December 2024,
Accepted 18th March 2025

DOI: 10.1039/d4nr05158k

rsc.li/nanoscale

Ultrasmall gold nanoclusters (AuNCs) with photoluminescence in the second near-infrared region (NIR-II) have emerged as promising probes for *in vivo* biomedical applications. However, it remains a challenge to utilize NIR-II-emitting AuNCs for imaging brain glioblastoma (GBM), which is highly lethal and hard to diagnose in time. Herein, we have presented systematic investigations on the brain delivery and GBM targeting efficacies of NIR-II-emitting AuNCs protected by different ligands. We first synthesized four types of AuNCs with surface coatings of small thiolated ligands and proteins, and then studied their *in vitro* penetration capability into the blood–brain barrier (BBB) and *in vivo* GBM targeting performances. It was found that the BBB permeability of AuNCs determined by the *in vitro* transwell model was not evidently affected by the surface ligands. Significantly, AuNCs protected by albumin exhibited notably extended blood circulation and less skull binding compared to those protected by small ligands, enabling superior *in vivo* brain GBM-targeted NIR-II PL imaging. We also modified the albumin–AuNCs with targeting peptides to improve *in vivo* imaging contrast. Additionally, AuNCs had negligible toxic effects on major organs as well as brain tissues and neurons, corroborating their good biocompatibility. This study examined the surface engineering of NIR-II luminescent AuNCs for brain GBM targeting, which may offer insights into the future design of AuNCs for bioapplications.



## Introduction

Primary glioblastoma (GBM) is one of the most common and lethal intracranial malignant tumors, due to its high mortality and poor prognosis.[1–3] At present, the clinical diagnosis of GBM is generally based on the use of brain computed tomography (CT) and magnetic resonance imaging (MRI), which however may encounter low spatial resolution, insensitivity, or radiation risk.[4] To satisfy the practical requirements of precise surgery and therapeutic monitoring, imaging techniques with real-time and high-contrast imaging capabilities are always desired.[5–7] In recent years, investigators have paid increasing attention to *in vivo* photoluminescence (PL) imaging techniques in the second near-infrared (NIR-II) region,[8–11] which has significant advantages in terms of imaging sensitivity and resolution as well as light penetration depth, compared to the ultraviolet–visible[12,13] and first NIR (NIR-I) region.[14–17] Through-skull NIR-II PL imaging is therefore considered promising for the diagnosis and therapeutic monitoring of GBM and other brain diseases.[18–20]

In order to achieve high-quality NIR-II PL imaging of GBM, it is necessary to select appropriate luminescent probes with low toxicity to the brain. As a class of generally recognized low-toxicity materials, gold materials with unique physicochemical properties have been widely studied in bioimaging and therapy fields.[21–24] For example, gold complexes are utilized in the clinic for the treatment of arthritis, tumors, neurological disorders, *etc.*[25–29] In this scenario, the emerging NIR-II luminescent ultrasmall gold nanoclusters (AuNCs) might be a solution for *in vivo* imaging of brain GBM. However, it is essential to consider whether they can effectively traverse the blood–brain barrier (BBB), which can prevent exogenous substances from entering the brain while ensuring nutrient supply and substance exchange.[30,31] Although there are some reports on the brain-related applications of visible/NIR-I-emitting AuNCs, the brain delivery efficiencies are still not enough and such traditional AuNCs may differ from NIR-II AuNCs in material compositions and surface properties as well as the related biofate and brain delivery capabilities.[7,32] Notably, there have been no reports on brain GBM imaging using NIR-II luminescent AuNCs so far.

[a]*MOE Key Laboratory for Analytical Science of Food Safety and Biology, College of Chemistry, Fuzhou University, Fuzhou, Fujian 350116, China. E-mail: xrsong@fzu.edu.cn*
[b]*School of Medical Imaging, Fujian Medical University, Fuzhou, Fujian 350122, China. E-mail: lishihua@fjmu.edu.cn*
[c]*Fujian Science & Technology Innovation Laboratory for Optoelectronic Information of China, Fuzhou 350108, China*

† Electronic supplementary information (ESI) available. See DOI: https://doi.org/10.1039/d4nr05158k

Herein, we demonstrate the rational engineering of NIR-II luminescent AuNCs for achieving high-efficiency brain GBM-targeted imaging.[33–35] We first synthesized AuNCs with surface coatings of glutathione (GSH), cyclodextrin (CD), *N*-acetyl cysteine (NAC), and bovine serum albumin (BSA), which are hereafter denoted as GNCs, CNCs, NNCs, and BNCs, respectively. These four kinds of AuNCs possessed NIR-II PL at around 1050 nm and high water dispersibility. By using the classical transwell model,[36,37] we found that the penetration rates and tumor cell uptake amounts of the four AuNCs differed only slightly, as revealed by *in vitro* NIR-II PL imaging and metal content analysis. This indicated the plausible weak correlation between surface coatings and *in vitro* BBB permeability of the ultrasmall AuNCs. Significantly, BNCs enabled more efficient GBM targeting and NIR-II PL imaging in orthotopic mouse brain GBM models, compared to GNCs, CNCs, and NNCs. The enhanced brain GBM targeting of BNCs was found to be caused by their much longer blood circulation and lower skull accumulation attributes. Moreover, we can additionally decorate BNCs with targeting peptides,[38–40] achieving approximately 2-fold contrast improvement in NIR-II PL imaging of GBM *in vivo*, relative to that in healthy mice. Besides, we systematically studied the brain biocompatibility of BNCs and confirmed their negligible toxicity effects on neurological functions and brain tissues. This work unravels the surface coating effects of NIR-II luminescent AuNCs on their brain delivery and GBM targeting efficiencies, which could offer insights into brain-related imaging and therapy research.

## Results and discussion

In view of the fact that the biofate of AuNCs is closely related to their surface properties, we tried to synthesize AuNCs with varying surface ligands, including GSH, CD, NAC, and BSA. The AuNCs were synthesized through a sodium borohydride mediated one-pot reduction method in alkaline environments.[41–43] Transmission electron microscopy (TEM, Fig. 1a) indicated that these clusters had ultrasmall sizes of approximately 2 nm. The hydrodynamic diameters (HDs) were slightly increased in the AuNCs carrying larger-sized ligands, and BNCs had the largest HDs of about 2.5 nm (Fig. 1b). Zeta potentials of these AuNCs were all negative due to the presence of carboxyl and/or hydroxyl groups in the ligands, which also endowed them with good water dispersibility (Fig. S1†). We also tried to examine the molecular information about AuNCs by performing electrospray ionization mass spectrometry (ESI-MS) or matrix-assisted laser desorption ionization time-of-flight mass spectrometry (MALDI-TOF MS). As illustrated in Fig. S2† (measured by ESI-MS), GNCs had three prominent sets of MS peaks with charges of $6^-$, $5^-$, and $4^-$, respectively (Fig. S2a†). In each charge state, four main components can be observed, accompanied by some other weak peaks. Taking the sets of charge $4^-$ as an example, the peaks at $m/z$ = 1727.28, 1754.56, 1803.20, and 2055.70 can be assigned to $[Au_{18}(SG)_{11}\text{-}4H]^{4-}$, $[Au_{17}(SG)_{12}\text{-}4H]^{4-}$, $[Au_{18}(SG)_{12}\text{-}4H]^{4-}$, and $[Au_{20}(SG)_{14}\text{-}4H]^{4-}$, respectively (Fig. S2b–e†). Also, the simulated isotope patterns matched the experimental data well. Thus, the synthesized GNCs may be described as $Au_{17-20}(SG)_{11-14}$.[44–46] As for the ESI-MS data of NNCs (Fig. S3†), two prominent sets of peaks with charges of $6^-$ and $5^-$ were observed, each of which included four main components. Through analyzing charge $6^-$, the peaks at $m/z$ = ~1786.35, 1841.02, 1900.86, and 1986.50 can be assigned to $[Au_{36}(NAC)_{22} + 2Na\text{-}8H]^{6-}$, $[Au_{36}(NAC)_{24} + 2Na\text{-}8H]^{6-}$, $[Au_{37}(NAC)_{25} + 2Na\text{-}8H]^{6-}$, and $[Au_{38}(NAC)_{27} + 2Na\text{-}8H]^{6-}$, respectively. Therefore, NNCs can be approximately described as $Au_{36-38}(NAC)_{22-27}$. We also attempted to determine the atomic number of CNCs by ESI-MS analysis. However, it is hard to clearly figure out the charge states and molecular weights. Also, we have failed to obtain precise atomic information about BNCs from MALDI-TOF MS. This

**Xiaorong Song**

*Xiaorong Song obtained his Ph. D. degree in analytical chemistry from Fuzhou University in 2017. He completed his visiting research at the National University of Singapore, followed by postdoctoral research at the Fujian Institute of Research on the Structure of Matter, Chinese Academy of Sciences. He is currently a Professor of Chemistry at Fuzhou University. His research focuses on diagnostic and therapeutic applications of luminescent materials especially lanthanide probes and metal nanoclusters. He has published more than 50 papers in journals like Angew. Chem. Int. Ed., Adv. Mater., Nano Lett., ACS Nano, Adv. Funct. Mater. and Anal. Chem.*

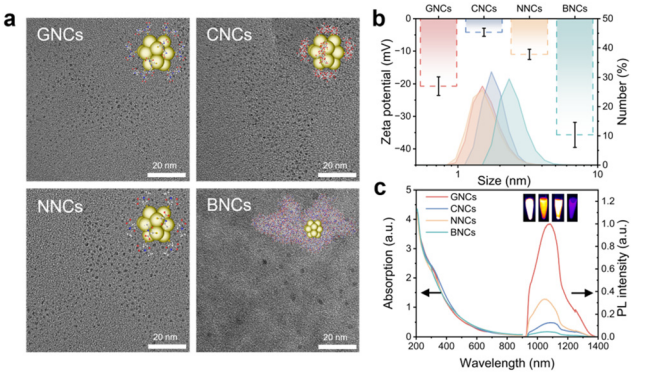


**Fig. 1** Characterization of GNCs, CNCs, NNCs, and BNCs. (a) TEM images of GNCs, CNCs, NNCs, and BNCs. (b) Zeta potential (dash) and hydrodynamic sizes (solid) of these AuNCs. Data are presented as mean ± SD ($n$ = 3). (c) Absorption spectra and PL spectra (Ex. 808 nm) at the same Au concentration (0.2 mM) of these AuNCs. Inset: NIR-II PL images of GNCs, CNCs, NNCs, and BNCs (from left to right).

could be due to the fact that it is often challenging to obtain the atomic number of AuNCs protected by macromolecular ligands/proteins. Further studies of atomically precise synthesis methods may be needed.

In addition, the absorption spectra showed that all AuNCs exhibited broad absorption in visible and NIR regions (300–900 nm), differentiating them from large-sized (*e.g.*, >10 nm) Au nanoparticles with typical surface plasmon resonance absorption peaks (Fig. 1c). These AuNCs also exhibited NIR-II PL emission at around 1050 nm upon 808 nm excitation. The PL quantum yields (QYs) of GNCs, CNCs, NNCs, and BNCs were found to be approximately 0.55%, 0.17%, 0.30%, and 0.05%, respectively, by using IR-26 dye (QY = 0.05% in dimethyl sulfoxide) as a reference. The NIR-II PL imaging capabilities of these AuNCs were also verified, indicating their good bioimaging potential (inset, Fig. 1c).

To evaluate the BBB permeability of the obtained AuNCs, we established a transwell-based *in vitro* BBB model by culturing mouse brain microvascular endothelial cells (bEnd.3) and glioma cells (GL261) in the upper and bottom chambers, respectively (Fig. 2a). To confirm the construction of *in vitro* transwell BBB models, the trans-endothelial electrical resistance (TEER) value was monitored. The TEER value is considered as a vital indicator of cell layer integrity and permeability, and a high TEER value (*e.g.*, >150 Ω $cm^2$) can indicate the formation of an intact cell layer with proper intercellular tight junctions.[47–49] We then cultured the cells until TEER values reached up to >300 Ω $cm^2$ to guarantee successful construction of transwell models (Fig. S4†).[37,50] In addition, we used confocal laser scanning microscopy (CLSM) to examine the cell integrity. Through the co-staining of cell nuclei, lysosomes, and membranes, we can see that the cells were well cultured in the upper and bottom chambers (Fig. 2a and S5†). After culturing AuNCs with the cells in the upper chamber, we conducted NIR-II PL imaging to survey the BBB permeability. NIR-II PL images of the culture media in the bottom chamber brightened with prolonged incubation time, indicative of their gradual penetration through the cell layer (Fig. 2b). Moreover, we quantitatively detected the penetration rates by using inductively coupled plasma mass spectrometry (ICP-MS). Results showed that the four AuNCs have almost similar penetration rates of ~50% after 48 h of incubation (Fig. 2c). Besides, GL261 cells showed no obvious difference in the uptake of AuNCs, showing around 3% of the added dose (Fig. 2d). This suggests that the *in vitro* BBB permeability might not be significantly related to the surface coatings of AuNCs. Because the tight junctions (TJs) between endothelial cells (ECs) of the BBB have a gap of 4–6 nm,[51,52] the ultrasmall AuNCs (<2 nm) may be able to cross the BBB in a passive diffusion manner, resulting in weak effects of surface coatings on their BBB penetration efficiencies.[53,54] Furthermore, we evaluated the cytotoxicity of AuNCs by using cell counting kit-8 (CCK-8). Both bEnd.3 cells and GL261 cells had high cell viabilities, larger than 80% even after incubation with AuNCs at concentrations of 500 μM (on the basis of the Au element), indicating their low cytotoxicity (Fig. S6†).

We subsequently tried to figure out whether surface ligands on AuNCs could affect *in vivo* brain delivery and GBM targeting efficacies. To this end, we constructed *in situ* brain GBM models by utilizing an automatic stereotaxic instrument. All animal procedures were performed in accordance with the relevant laws and institutional guidelines and were approved

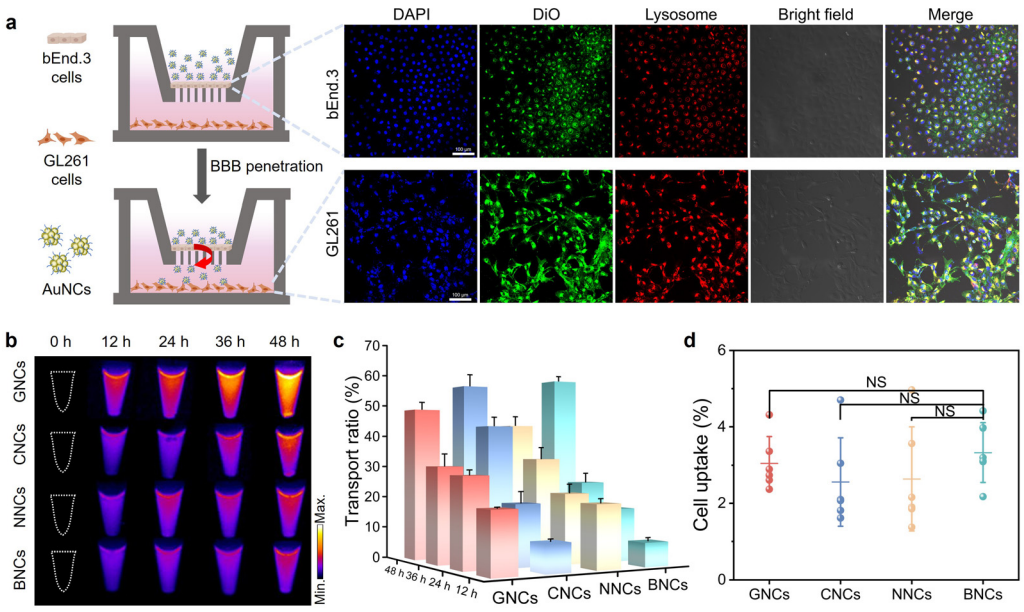


**Fig. 2** *In vitro* BBB penetration and tumor cell uptake studies. (a) Schematic illustration of the *in vitro* BBB model and CLSM images of bEnd.3 cells and GL261 cells. (b) NIR-II PL images of the culture media in the bottom chambers collected at different time points after adding AuNCs to the upper chambers. (c) Time-evolved transport ratios determined *via* dividing Au contents in the bottom chamber by the initially added Au contents. (d) Uptake of AuNCs by GL261 cells cultured in the bottom chamber. Statistical significance: NS ($P > 0.05$). Data are presented as mean ± SD ($n = 3$).

by the Animal Ethics Committee of Fuzhou University. The successful construction of the GBM models was revealed by brain tissue examinations and bioluminescence (BL) imaging (Fig. S7 and S8†). Experimentally, the orthotopic brain GBM models can be well obtained at 21 d post inoculation. Healthy mice and brain GBM-bearing mice were then intravenously injected with different AuNCs, respectively. At desired time points after injection, the mice were imaged by using an InGaAs camera under 808 nm excitation (200 mW $cm^{-2}$) (Fig. 3a). It can be seen that GNCs, CNCs, and NNCs were rapidly excreted into the bladder in a few minutes after injection into healthy and tumor-bearing mice, along with very low accumulation in the liver and other major organs (Fig. S9 and S10†). Particularly, strong NIR-II PL signals were observed in the mouse skull after injection of the three AuNCs, indicating their strong skull binding (Fig. 3b). This leads to low GBM targeting and poor diagnosis capability for brain GBM.[55] In contrast, BNCs showed a prolonged blood circulation time after the intravenous injection, allowing high-contrast *in vivo* blood vessel imaging within a few hours (Fig. S9 and S10†). More significantly, BNCs had low skull accumulation and the NIR-II PL signals in the healthy mouse brain gradually decreased as time prolonged.[56,57] The NIR-II PL signals in the brain regions of tumor-bearing mice gradually increased within 12 h (Fig. 3c). At 24 h post injection, about a 7-fold increase of NIR-II PL signals can be observed in the brain (relative to that before the injection of BNCs), as supported by NIR-II PL images of *ex vivo* tumor tissues (Fig. 3d and e). The gold content detected by ICP-MS also supported the enhanced accumulation (about 10 fold) in the brain GBM in BNC groups compared to that in the other three groups (Fig. 3f). Besides, BNCs obviously accumulated in major organs of mice (*e.g.*, liver and kidneys), consistent with the previous findings in BSA-based materials (Fig. S11†).[58] Therefore, BNCs facilitated enhanced *in vivo* brain GBM targeting compared to GNCs, CNCs, and NNCs. This could be mainly attributed to the prolonged blood circulation capability of BNCs (Fig. S12 and S13†), which permits their brain tumor accumulation after BBB penetration *in vivo*. The BBB penetration of BNCs was also verified by NIR-II PL imaging of *ex vivo* brain tissues, which showcased obvious signal enhancement after injection of BNCs (Fig. S14†). However, we also acknowledge that the NIR-II PL signals in brain tissues were not very high, probably owing to the limitations in the PL efficiency and BBB penetration capability of BNCs.

To further improve *in vivo* GBM targeting efficacy, we next modified BNCs with arginine–glycine–aspartic acid (RGD) targeting peptides that can actively target tumor cells expressing integrin.[38,59] The peptide was designed with a free thiol end to form a stable gold–sulfur bond on AuNCs,[39] resulting in RGD-modified BNCs (denoted as BNCs-RGD) (Fig. 4a).[58] By using an ultra-performance liquid chromatography mass spectrometer (see the Experimental section in the ESI† for details), the molar ratio of albumin/RGD was determined to be ~0.5 (Fig. S15†).[60] The particle size showed negligible changes, while the surface negative charge was slightly decreased after RGD modification (Fig. 4b and S16†). Meanwhile, the PL inten-

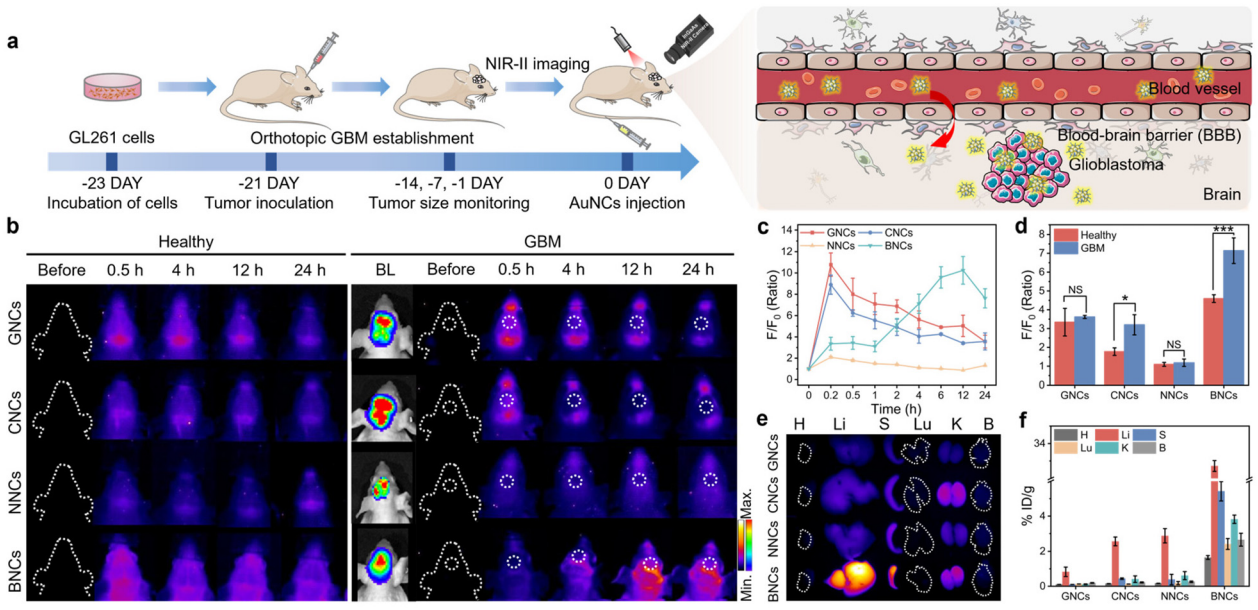


**Fig. 3** *In vivo* NIR-II PL imaging of orthotopic brain GBM. (a) Schematic of the construction of orthotopic brain GBM models in mice and NIR-II PL imaging by injecting AuNCs. The BBB penetration and GBM targeting are illustrated. (b) NIR-II PL imaging of healthy mice and orthotopic GBM-bearing mice post injection of GNCs, CNCs, NNCs, and BNCs, respectively (808 nm excitation). (c) Corresponding PL intensity changes of the tumor regions (white circles) as determined using ImageJ software ($F_0$: PL intensity before injection). Data are presented as mean ± SD ($n$ = 3). (d) *In vivo* NIR-II PL intensity comparisons of tumor regions at 24 h post injection. Statistical significance: NS ($P > 0.05$), *$P < 0.05$, **$P < 0.01$, ***$P < 0.005$. (e) NIR-II PL images and (f) Au contents of *ex vivo* major organs (*i.e.*, heart (H), liver (Li), spleen (S), lungs (Lu), and kidneys (K)) and brain tissues (B) collected from GBM-bearing mice at 24 h post injection of these AuNCs. Data are presented as mean ± SD ($n$ = 3).

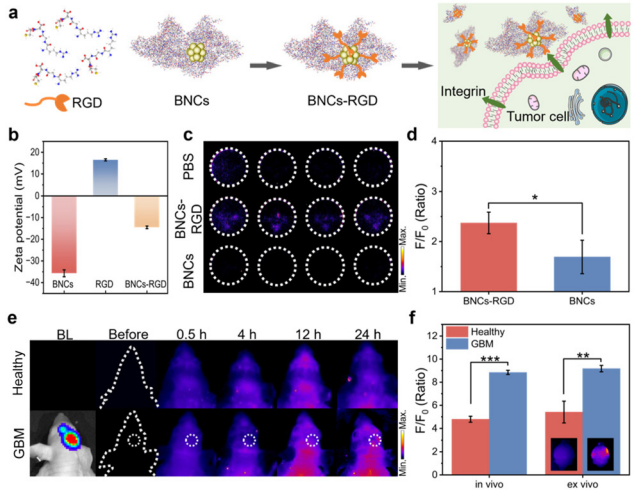


**Fig. 4** Orthotopic brain GBM-targeted NIR-II PL imaging by using BNCs-RGD. (a) Schematic illustration of BNCs-RGD and the specific targeting of integrin expressed on tumor cells. (b) Zeta potential of BNCs, RGD, and BNCs-RGD, respectively. (c) NIR-II PL images of GL261 cells after incubation with PBS, BNCs, and BNCs-RGD for 24 h. (d) Corresponding PL intensity changes in different groups ($F_0$: PL intensity of PBS group). (e) NIR-II PL imaging of healthy mice and GBM-bearing mice after the injection of BNCs-RGD. (f) PL intensity changes of *in vivo* and *ex vivo* brain tissues in healthy and tumor-bearing mice at 24 h post injection of BNCs-RGD ($F_0$: PL intensity before injection). Inset: NIR-II PL images of *ex vivo* brain tissues of healthy mice and GBM-bearing mice. Data are presented as mean ± SD ($n$ = 3). Statistical significance: NS ($P$ > 0.05), *$P$ < 0.05, **$P$ < 0.01, ***$P$ < 0.005.

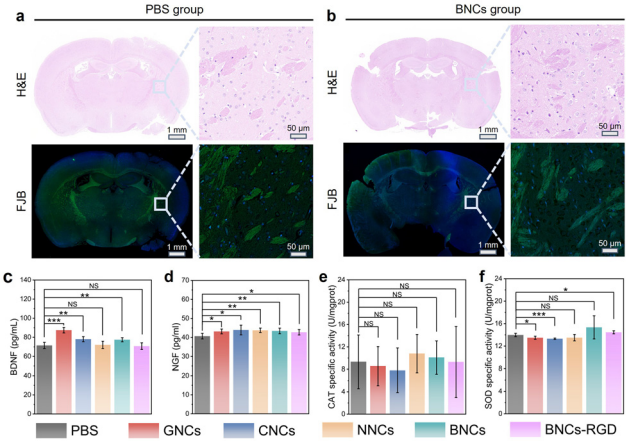


**Fig. 5** Biocompatibility evaluation of AuNCs. H&E staining images and FJB staining images of the brain tissues of healthy mice at 24 h post injection of (a) PBS and (b) BNCs. The determined levels of (c) BDNF, (d) NGF, (e) CAT activity, and (f) SOD activity in the brain tissues of healthy mice at 24 h post injection of PBS, GNCs, CNCs, NNCs, BNCs, and BNCs-RGD, respectively. Data are presented as mean ± SD ($n$ = 3). Statistical significance: NS ($P$ > 0.05), *$P$ < 0.05, **$P$ < 0.01, ***$P$ < 0.005.

sity of BNCs was increased 2.5 times after RGD modification, likely due to the presence of electron-rich atoms and groups (*e.g.*, carboxyl and amide groups) in the RGD ligand that could facilitate PL.[61–64] The tumor targeting effect of BNCs-RGD was then studied *in vitro*. Based on NIR-II PL imaging of cells, the uptake amount of BNCs-RGD in GL261 cells was found to be 1.5 times that of the BNC group, suggesting enhanced tumor cell uptake after RGD modification (Fig. 4c and d). We then injected BNCs-RGD into healthy mice and brain GBM-bearing mice *via* the tail vein for *in vivo* NIR-II PL imaging (Fig. S17 and S18†). Significantly, enhanced NIR-II PL signals can be observed in brain GBM-bearing mice, showing a maximum PL increase of ~9 fold at 24 h post injection, while only weak PL signals were observed in the brain of healthy mice (Fig. 4e and f). Also, commercial indocyanine green (ICG) was intravenously injected into GBM-bearing mice and negligible NIR-II PL signals were detected in the brain (Fig. S19†).[65,66] These results thereby implied the good brain tumor targeting efficacy of BNCs-RGD.

In addition, we systematically evaluated the biocompatibility and safety of these AuNCs in mice. The routine blood tests were first conducted to examine the blood compatibility and toxicity to metabolism-related organs (*e.g.*, liver and kidneys). As shown in Fig. S20,† these AuNCs had no obvious cytotoxic effects on the blood and did not affect the renal and liver functions. Histological analysis of tissues (collected at 24 h post injection) confirmed the low toxicity and high tissue biocompatibility of these AuNCs (Fig. S21†). Considering the critical roles of the central nervous system, we also investigated the potential brain toxicity of BNCs by performing histological analyses of the brain tissues and the detection of brain function-related biomarkers.[67,68] As illustrated by hematoxylin and eosin (H&E) staining, there were no signs of pathological damage to the brain tissues after BNC treatment (Fig. 5a and b). Additionally, Fluor-Jade B (FJB) staining, which can specifically bind to degenerating neurons, showed negligible existence of green fluorescence in the brain tissues of BNC-treated mice, suggesting negligible toxic effects of BNCs on the neurons. We then determined the levels of the brain-derived neurotrophic factor (BDNF) and nerve growth factor (NGF) in mice, which are important biomarkers associated with learning, memory, and others.[69,70] 24 h after the injection of AuNCs, the levels of these biomarkers in the isolated brain tissues were all within the normal ranges, indicating no evident toxic effects on the central nervous system (Fig. 5c and d). As essential antioxidant enzymes, superoxide dismutase (SOD) and catalase (CAT) are vital for maintaining the cerebral health and function.[71] No significant changes in the enzymatic activities were observed in the isolated brain tissues of AuNC-injected mice, in comparison with those in the PBS-treated mice (Fig. 5e and f). To sum up, these results indicated that AuNCs had low toxicity to the brain and BNCs could be promising as imaging probes for brain applications.

## Conclusions

In summary, we have systematically studied *in vitro* BBB permeability and *in vivo* brain GBM targeting efficacy of surface-engineered AuNCs, developing BNCs for effective NIR-II PL imaging of brain GBM. Four kinds of NIR-II-emitting AuNCs were synthesized by using small thiolated ligands and pro-

teins. We found that the BBB permeability of AuNCs was not evidently affected by the surface ligands plausibly due to their ultrasmall sizes. In comparison with AuNCs protected by small ligands, BNCs had notably extended blood circulation and less skull binding features, enabling superior *in vivo* brain GBM-targeted NIR-II PL imaging. We also successfully modified BNCs with targeting peptides to further improve the targeting efficacy and imaging contrast. Besides, we revealed negligible toxic effects of AuNCs on major organs as well as brain tissues and neurons, which corroborates their good biocompatibility. This study is therefore anticipated to provoke further research interest in designing AuNCs for brain-related bioimaging and therapy applications.

## Author contributions

This project was supervised by S.L., X.S., and H.Y.; S.T., S.L., and X.S. designed experiments, S.T. and J.L. conducted experiments and analyzed the data, Y.C. and X.X. helped with data recording and analysis, S.L., X.S., and H.Y. revised the manuscript. All authors took part in the discussion of results and manuscript preparation.

## Data availability

The data supporting this article have been included as part of the ESI.†

## Conflicts of interest

There are no conflicts to declare.

## Acknowledgements

This research was supported by the National Natural Science Foundation of China (No. 22027805, 22274024, and 22404022), the Major Project of Science and Technology of Fujian Province (No. 2020HZ06006), the Natural Science Foundation of Fujian Province (No. 2024J01701), and the Start-up Fund for Scientific Research of Fujian Medical University (No. XRCZX2024008).

## References

1 S. B. Rikan, A. S. Azar, A. Naemi, J. B. Mohasefi, H. Pirnejad and U. K. Wiil, *Sci. Rep.*, 2024, **14**, 2371.
2 E. I. Styliara, L. G. Astrakas, G. Alexiou, V. G. Xydis, A. Zikou, G. Kafritsas, S. Voulgaris and M. I. Argyropoulou, *Curr. Oncol.*, 2024, **31**, 2233–2243.
3 R. Mathur, Q. Wang, P. G. Schupp, A. Nikolic, S. Hilz, C. Hong, N. R. Grishanina, D. Kwok, N. O. Stevers, Q. Jin, M. W. Youngblood, L. A. Stasiak, Y. Hou, J. Wang, T. N. Yamaguchi, M. Lafontaine, A. Shai, I. V. Smirnov, D. A. Solomon, S. M. Chang, S. L. Hervey-Jumper, M. S. Berger, J. M. Lupo, H. Okada, J. J. Phillips, P. C. Boutros, M. Gallo, M. C. Oldham, F. Yue and J. F. Costello, *Cell*, 2024, **187**, 446–463.
4 K. Connor, E. Conroy, K. White, L. P. Shiels, S. Keek, A. Ibrahim, W. M. Gallagher, K. J. Sweeney, J. Clerkin, D. O'Brien, J. B. Cryan, P. J. O'Halloran, J. Heffernan, F. Brett, P. Lambin, H. C. Woodruff and A. T. Byrne, *Sci. Rep.*, 2024, **14**, 2720.
5 Z. Yu, B. Musnier, K. D. Wegner, M. Henry, B. Chovelon, A. Desroches-Castan, A. Fertin, U. Resch-Genger, S. Bailly, J.-L. Coll, Y. Usson, V. Josserand and X. Le Guével, *ACS Nano*, 2020, **14**, 4973–4981.
6 F. Ren, Z. Jiang, M. Han, H. Zhang, B. Yun, H. Zhu and Z. Li, *View*, 2021, **2**, 20200128.
7 R. Thangam, R. Paulmurugan and H. Kang, *Nanomaterials*, 2021, **12**, 18.
8 K. Zhang, F. R. Chen, L. Wang and J. Hu, *Small*, 2023, **19**, 2206044.
9 H. Liu, G. Hong, Z. Luo, J. Chen, J. Chang, M. Gong, H. He, J. Yang, X. Yuan, L. Li, X. Mu, J. Wang, W. Mi, J. Luo, J. Xie and X. D. Zhang, *Adv. Mater.*, 2019, **31**, 1901015.
10 S. Ni, Y. Liu, S. Tong, S. Li and X. Song, *J. Anal. Test.*, 2023, **7**, 260–271.
11 S. Liang, D. Hu, G. Li, D. Gao, F. Li, H. Zheng, M. Pan and Z. Sheng, *Sci. Bull.*, 2022, **67**, 2316–2326.
12 K. Yang, Y. Yang, D. Sun, S. Li, X. Song and H. Yang, *Sci. China Mater.*, 2023, **66**, 4090–4099.
13 X. Song, M. Li, S. Ni, K. Yang, S. Li, R. Li, W. Zheng, D. Tu, X. Chen and H. Yang, *Nano Lett.*, 2023, **23**, 1878–1887.
14 A. Yahia-Ammar, D. Sierra, F. Mérola, N. Hildebrandt and X. Le Guével, *ACS Nano*, 2016, **10**, 2591–2599.
15 T. Chen, H. Lin, Y. Cao, Q. Yao and J. Xie, *Adv. Mater.*, 2021, **34**, 2103918.
16 L. Liang, J. Chen, K. Shao, X. Qin, Z. Pan and X. Liu, *Nat. Mater.*, 2023, **22**, 289–304.
17 H. Chen, B. Ding, P. A. Ma and J. Lin, *Adv. Drug Delivery Rev.*, 2022, **188**, 114414.
18 Y. Du, S. Ni, Q. Ma, X. Song and H. Yang, *Coord. Chem. Rev.*, 2023, **496**, 215401.
19 D. Huang, Q. Wang, Y. Cao, H. Yang, M. Li, F. Wu, Y. Zhang, G. Chen and Q. Wang, *ACS Nano*, 2023, **17**, 5033–5046.
20 N. Yin, Y. Wang, Y. Cao, Y. Huang, L. Jin, S. Zhang, J. Liu, T. Zhang, Z. Lv, Y. Liu, S. Song, D. Wang and H. Zhang, *Nano Today*, 2022, **46**, 101619.
21 J. Yang, F. Yang, C. Zhang, X. He and R. Jin, *ACS Mater. Lett.*, 2022, **4**, 1279–1296.
22 E. Porret, X. Le Guével and J.-L. Coll, *J. Mater. Chem. B*, 2020, **8**, 2216–2232.
23 L. Shang, J. Xu and G. U. Nienhaus, *Nano Today*, 2019, **28**, 100767.
24 D. Sang, X. Luo and J. Liu, *Nano-Micro Lett.*, 2023, **16**, 44.
25 G. Yang, K. Liu, Y. Wang, X. Pan, J. Ye, Y. Li, F. Du, T. Feng and X. Yuan, *Aggregate*, 2023, **5**, e435.
26 F. Xiao, Y. Chen, J. Qi, Q. Yao, J. Xie and X. Jiang, *Adv. Mater.*, 2023, **35**, 2210412.

27 G. Yang, X. Mu, X. Pan, Y. Tang, Q. Yao, Y. Wang, F. Jiang, F. Du, J. Xie, X. Zhou and X. Yuan, *Chem. Sci.*, 2023, **14**, 4308–4318.
28 W. Cheng, Y.-L. Su, H.-H. Hsu, Y.-H. Lin, L.-A. Chu, W.-C. Huang, Y.-J. Lu, C.-S. Chiang and S.-H. Hu, *ACS Nano*, 2022, **16**, 4014–4027.
29 N. Perets, O. Betzer, R. Shapira, S. Brenstein, A. Angel, T. Sadan, U. Ashery, R. Popovtzer and D. Offen, *Nano Lett.*, 2019, **19**, 3422–3431.
30 J. Li, M. Zheng, O. Shimoni, W. A. Banks, A. I. Bush, J. R. Gamble and B. Shi, *Adv. Sci.*, 2021, **8**, 2101090.
31 B. A. Buil, C. Tackenberg and R. Rust, *Brain*, 2023, **146**, 823–841.
32 Y. Cheng, Q. Dai, R. A. Morshed, X. Fan, M. L. Wegscheid, D. A. Wainwright, Y. Han, L. Zhang, B. Auffinger, A. L. Tobias, E. Rincón, B. Thaci, A. U. Ahmed, P. C. Warnke, C. He and M. S. Lesniak, *Small*, 2014, **10**, 5137–5150.
33 S. Li, Q. Ma, C. Wang, K. Yang, Z. Hong, Q. Chen, J. Song, X. Song and H. Yang, *Anal. Chem.*, 2022, **94**, 2641–2647.
34 X. Song, W. Zhu, X. Ge, R. Li, S. Li, X. Chen, J. Song, J. Xie, X. Chen and H. Yang, *Angew. Chem., Int. Ed.*, 2020, **60**, 1306–1312.
35 Y. Yu, Z. Luo, C. S. Teo, Y. N. Tan and J. Xie, *Chem. Commun.*, 2013, **49**, 9740–9742.
36 D. Qi, H. Lin, B. Hu and Y. Wei, *J. Controlled Release*, 2023, **358**, 78–97.
37 A. Wolff, M. Antfolk, B. Brodin and M. Tenje, *J. Pharm. Sci.*, 2015, **104**, 2727–2746.
38 H. Javid, M. A. Oryani, N. Rezagholinejad, A. Esparham, M. Tajaldini and M. Karimi-Shahri, *Cancer Med.*, 2024, **13**, e6800.
39 G. Liang, X. Jin, S. Zhang and D. Xing, *Biomaterials*, 2017, **144**, 95–104.
40 Y. Wu, D. Hu, D. Gao, C. Liu, H. Zheng and Z. Sheng, *Adv. Healthcare Mater.*, 2022, **11**, 2202379.
41 X. Yuan, B. Zhang, Z. Luo, Q. Yao, D. T. Leong, N. Yan and J. Xie, *Angew. Chem., Int. Ed.*, 2014, **53**, 4623–4627.
42 Q. Dan, Z. Yuan, S. Zheng, H. Ma, W. Luo, L. Zhang, N. Su, D. Hu, Z. Sheng and Y. Li, *Pharmaceutics*, 2022, **14**, 1645.
43 L. Tang, X. Zeng, H. Zhou, C. Gui, Q. Luo, W. Zhou, J. Wu, Q. Li, Y. Li and Y. Xiao, *Chem. Res. Chin. Univ.*, 2021, **37**, 934–942.
44 Q. Yao, M. Zhu, Z. Yang, X. Song, X. Yuan, Z. Zhang, W. Hu and J. Xie, *Nat. Rev. Mater.*, 2024, **10**, 89–108.
45 H. Shan, J. Shi, T. Chen, Y. Cao, Q. Yao, H. An, Z. Yang, Z. Wu, Z. Jiang and J. Xie, *ACS Nano*, 2023, **17**, 2368–2377.
46 Z. Luo, X. Yuan, Y. Yu, Q. Zhang, D. T. Leong, J. Y. Lee and J. Xie, *J. Am. Chem. Soc.*, 2012, **134**, 16662–16670.
47 X. Ma, L. Kuang, Y. Yin, L. Tang, Y. Zhang, Q. Fan, B. Wang, Z. Dong, W. Wang, T. Yin and Y. Wang, *ACS Nano*, 2023, **17**, 2341–2355.
48 S. I. Ahn, Y. J. Sei, H.-J. Park, J. Kim, Y. Ryu, J. J. Choi, H.-J. Sung, T. J. MacDonald, A. I. Levey and Y. Kim, *Nat. Commun.*, 2020, **11**, 175.
49 K. B. Johnsen, M. Bak, P. J. Kempen, F. Melander, A. Burkhart, M. S. Thomsen, M. S. Nielsen, T. Moos and T. L. Andresen, *Theranostics*, 2018, **8**, 3416–3436.
50 H. Chen, J. Ji, L. Zhang, C. Luo, T. Chen, Y. Zhang, C. Ma, Y. Ke and J. Wang, *Small*, 2024, **20**, 2306714.
51 E. Nance, S. H. Pun, R. Saigal and D. L. Sellers, *Nat. Rev. Mater.*, 2021, **7**, 314–331.
52 S. Zha, H. Liu, H. Li, H. Li, K.-L. Wong and A. H. All, *ACS Nano*, 2024, **18**, 1820–1845.
53 J. Zhang, T. Yang, W. Huang, Y. Yu and T. Sun, *Curr. Med. Chem.*, 2022, **29**, 6063–6083.
54 H. Sela, H. Cohen, P. Elia, R. Zach, Z. Karpas and Y. Zeiri, *J. Nanobiotechnol.*, 2015, **13**, 1–9.
55 D. Li, Q. Liu, Q. Qi, H. Shi, E. C. Hsu, W. Chen, W. Yuan, Y. Wu, S. Lin, Y. Zeng, Z. Xiao, L. Xu, Y. Zhang, T. Stoyanova, W. Jia and Z. Cheng, *Small*, 2020, **16**, 2003851.
56 S. Lee, C. Lee, S. Park, K. Lim, S. S. Kim, J. O. Kim, E. S. Lee, K. T. Oh, H.-G. Choi and Y. S. Youn, *Int. J. Pharm.*, 2018, **553**, 363–374.
57 D.-H. Hu, Z.-H. Sheng, P.-F. Zhang, D.-Z. Yang, S.-H. Liu, P. Gong, D.-Y. Gao, S.-T. Fang, Y.-F. Ma and L.-T. Cai, *Nanoscale*, 2013, **5**, 1624–1628.
58 C. Zhang, N. Zhang, W. Niu, R. Li, Y. Liu, Y. Mu, C. Xu, Q. Yao and X. Gao, *Nano Today*, 2024, **55**, 102195.
59 J. Mo, L. He, B. Ma and T. Chen, *ACS Appl. Mater. Interfaces*, 2016, **8**, 6811–6825.
60 Q. Luo, H. Zhang, Y. Zhou, Z. Liu and Z. Cai, *Rapid Commun. Mass Spectrom.*, 2021, **35**, e9117.
61 W. Wang, Y. Kong, J. Jiang, Q. Xie, Y. Huang, G. Li, D. Wu, H. Zheng, M. Gao, S. Xu, Y. Pan, W. Li, R. Ma, M. X. Wu, X. Li, H. Zuilhof, X. Cai and R. Li, *Angew. Chem., Int. Ed.*, 2020, **59**, 22431–22435.
62 F. Bertorelle, K. D. Wegner, M. P. Bakulić, H. Fakhouri, C. Comby-Zerbino, A. Sagar, P. Bernadó, U. Resch-Genger, V. Bonačić-Koutecký, X. Le Guével and R. Antoine, *Chem. – Eur. J.*, 2022, **28**, e202200570.
63 M. Guo, G. Zhang, R. Zhao, H. Ma, Y. Yan, S. Yang, J. Meng, Y. Huang, X.-D. Zhang, H. Wang and R. Zhang, *ACS Appl. Nano Mater.*, 2023, **6**, 15945–15958.
64 Z. Wu and R. Jin, *Nano Lett.*, 2010, **10**, 2568–2573.
65 D. Zhang, S. Tian, Y. Liu, M. Zheng, X. Yang, Y. Zou, B. Shi and L. Luo, *Nat. Commun.*, 2022, **13**, 6835.
66 M. Zhu, Z. Sheng, Y. Jia, D. Hu, X. Liu, X. Xia, C. Liu, P. Wang, X. Wang and H. Zheng, *ACS Appl. Mater. Interfaces*, 2017, **9**, 39249–39258.
67 M. Miranda, J. F. Morici, M. B. Zanoni and P. Bekinschtein, *Front. Cell. Neurosci.*, 2019, **13**, 472800.
68 S.-K. Sims, B. Wilken-Resman, C. J. Smith, A. Mitchell, L. McGonegal, C. Sims-Robinson and G. Delevati Colpo, *Neural Plast.*, 2022, **2022**, 1–15.
69 M. Irfan, J. H. Kim, R. E. Druzinsky, S. Ravindran and S. Chung, *Sci. Rep.*, 2022, **12**, 2042.
70 M. Irfan and S. Chung, *Sci. Rep.*, 2023, **13**, 74.
71 G. K. Ferreira, E. Cardoso, F. S. Vuolo, L. S. Galant, M. Michels, C. L. Gonçalves, G. T. Rezin, F. Dal-Pizzol, R. Benavides, G. Alonso-Núñez, V. M. Andrade, E. L. Streck and M. M. S. Paula, *Mater. Sci. Eng., C*, 2017, **79**, 748–755.

 